Flower-like hydrogenated $TiO_2(B)$ nanostructures as anode materials for high-performance lithium ion batteries

Zhonghua Zhang, Zhenfang Zhou, Sen Nie, Honghu Wang, Hongrui Peng, Guicun Li[*], Kezheng Chen[*]

Laboratory of Functional and Biological Nanomaterials, College of Materials Science and Engineering, Qingdao University of Science and Technology, Qingdao 266042, China

HIGHLIGHTS

- $H-TiO_2(B)$ nanostructures are obtained by the solvothermal and hydrogenation method.
- The thin $TiO_2(B)$ nanosheets are advantageous for the Li^+ transport.
- Ti^{3+} species in $TiO_2(B)$ structure can in situ monitor its electrical conductivity.
- $H-TiO_2(B)$ nanostructures exhibited excellent electrochemical performances.

GRAPHICAL ABSTRACT
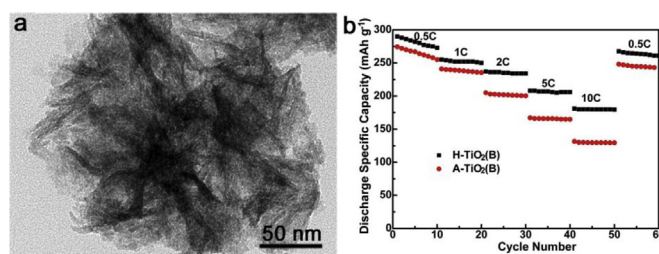
ARTICLE INFO

ABSTRACT

Flower-like hydrogenated $TiO_2(B)$ nanostructures have been synthesized via a facile solvothermal approach combined with hydrogenation treatment. The obtained $TiO_2(B)$ nanostructures show uniform and hierarchical flower-like morphology with a diameter of 124 ± 5 nm, which are further constructed by primary nanosheets with a thickness of 10 ± 1.2 nm. The Ti^{3+} species and/or oxygen vacancies are well introduced into the structures of $TiO_2(B)$ after hydrogen reduction, resulting in an enhancement in the electronic conductivity (up to 2.79×10^{-3} S cm^{-1}) and the modified surface electrochemical activity. When evaluated for lithium storage capacity, the hydrogenated $TiO_2(B)$ nanostructures exhibit enhanced electrochemical energy storage performances compared to the pristine $TiO_2(B)$ nanostructures, including high capacity (292.3 mA h g^{-1} at 0.5C), excellent rate capability (179.6 mA h g^{-1} at 10C), and good cyclic stability (98.4% capacity retention after 200 cycles at 10C). The reasons for these improvements are explored in terms of the increased electronic conductivity and the facilitation of lithium ion transport arising from the introduction of oxygen vacancies and the unique flower-like morphologies.

© 2014 Elsevier B.V. All rights reserved.

1. Introduction

Rechargeable lithium ion batteries are receiving great research interest due to their wide range of applications in portable electrical devices, stationary energy storage systems and high-power electric vehicles, etc [1–4]. Nowadays, further development of advanced electrode materials with high security, high energy density, long cycle life and good rate capability is necessary [4–6]. Ti-based compounds, such as anatase TiO_2 [7,8], rutile TiO_2 [9], $TiO_2(B)$ [10,11], and $Li_4Ti_5O_{12}$ [12,13], have been widely investigated as lithium ion battery anode materials since they exhibit excellent cycling reversibility, improved safety and better rate capability compared with graphite. $TiO_2(B)$, possessing more open channels in the lattice and featuring a unique pseudocapacitive process,

* Corresponding authors. Tel./fax: +86 532 84022814.
  E-mail addresses: guicunli@qust.edu.cn (G. Li), kchen@qust.edu.cn (K. Chen).

exhibits higher reversible capacity and faster charge–discharge capability [10,14–16]. However, the high-rate electrochemical properties of TiO₂(B) are significantly restricted by the low electronic conductivity and diffusion coefficient of Li⁺.

In recent years, morphology tailoring and size controls are especially important for TiO₂(B) to receive desirable high-rate lithium ion storage performances through reducing the diffusion path of Li⁺. TiO₂(B) nanostructures, such as nanoparticles [17], nanosheets [18], nanotubes [19], and nanowires [20], have been demonstrated as promising electrodes for lithium ion batteries. Nowadays, it is demonstrated that flower-like nanostructures exhibit high surface area and larger open pore for fast lithium diffusion, resulting in remarkable rate behavior as electrode materials for lithium ion batteries [21–23]. Che et al. reported nanosheet-constructed porous TiO₂(B) for advanced lithium ion batteries [18]. The reduced size shortens the transport paths of electrons and lithium ions, and simultaneously provides greater electrode/electrolyte contact area.

TiO₂(B), like other Ti-based compounds, also has a poor electronic conductivity when employed as an anode for lithium ion batteries. For Li₄Ti₅O₁₂ and other polymorphs of TiO₂, such as anatase and rutile, many attempts have been made on incorporating a second conductive phase to improve their electronic conductivity [13]. However, few similar studies for TiO₂(B) have been reported since most attempts involve high temperature treatments, which are not feasible for TiO₂(B) due to its metastable thermodynamics [13]. In addition, a large amount of conducting additives further reduces the volumetric energy density of TiO₂(B) electrode materials [24]. It is still a great challenge to fundamentally improve the electronic conductivity and pseudocapacitive behavior of TiO₂(B). Very recently, the introduction of oxygen vacancies and/or self-doping of Ti³⁺ into the TiO₂ lattice have proved to be a promising method to address these problems [25–28]. Our group reported a mesoporous hydrogenated anatase TiO₂ microspheres for high rate capability lithium ion batteries, which showed twice the rate capability compared to that of mesoporous anatase TiO₂ microspheres [28]. Sun et al. demonstrate that anatase TiO₂ with an electro-conducting trivalent Ti deliver a high rate Li⁺ insertion and extraction [29]. However, the effects of the introduction of oxygen vacancies and/or self-doping of Ti³⁺ species into TiO₂(B) for high rate lithium ion batteries remain unknown. Herein, we developed a facile solvothermal method combined with hydrogenation treatment process for the synthesis of flower-like hydrogenated TiO₂(B) nanostructures (denoted as H-TiO₂(B)) as anode materials for high-performance lithium ion batteries. The hydrogen reduction process can effectively provide TiO₂(B) with Ti³⁺ species and/or oxygen vacancies, which highly increase its intrinsic electronic conductivity. As expected, the H-TiO₂(B) electrodes exhibit enhanced electrochemical properties, especially better rate capability, compared to the pristine TiO₂(B) electrodes.

2. Experimental

2.1. Synthesis of H-TiO₂(B)

All reagents were used without further purification. The flower-like hydrogenated TiO₂(B) nanostructures were prepared via a combined solvothermal method in combination with low temperature hydrogenation process. In a typical procedure, 5 mL of butyl titanate was dissolved in 30 mL of ethylene glycol with stirring for 5 min 1 mL of hydrochloric acid was dropped into the above solution with careful attention. After stirred for another 5 min, the transparent mixture was sealed in a 40 mL Teflon-lined autoclave and then kept at 150 °C for 4 h in an oven. After cooling down to room temperature, the obtained products were thoroughly washed

with ethanol for several times to remove impurities and then dried overnight at 80 °C. The dried white powder was calcined at 350 °C for 3 h under H₂ atmosphere to obtain H-TiO₂(B). For comparison, the pristine flower-like TiO₂(B) nanostructures without hydrogenation were also prepared by calcination at 350 °C for 3 h in air [denoted as A-TiO₂(B)].

2.2. Characterization

X-ray diffraction (XRD Rigaku D-max-γA XRD with Cu K$_\alpha$ radiation, $\lambda = 1.54178$ Å) from 10° to 80° was used to determine the phase composition of H-TiO₂(B) and A-TiO₂(B) nanostructures. The morphologies and sizes of both samples were investigated by a field-emission scanning electron microscopy (FE-SEM, JSM 6700F) and a transmission electron microscopy (TEM, JEOL 2100F). The X-ray photoelectron spectroscopy (XPS) analysis was performed on a Perkin–Elmer PHI 550 spectrometer with Al K$_\alpha$ (1486.6 eV) as the X-ray source. The electronic conductivity of TiO₂(B) sample was measured by a four-point probe method at room temperature.

2.3. Electrode fabrication and electrochemical testing

The electrochemical tests were carried out using CR2032-type coin cell at room temperature. The working electrodes were prepared by mixing the products, carbon black (Super-P), and poly(-vinyl difluoride) (PVDF) at a weight ratio of 70:10:20 and pasting onto pure Cu foil. Pure lithium foil was employed as the counter electrode and separated by a Celgard 2500 membrane separator. The electrolyte consisted of a solution of 1 mol L⁻¹ LiPF₆ in ethylene carbonate/dimethyl carbonate (1:1 by volume). A glove box filled with high purity argon gas was used to assemble cells. The galvanostatic discharge–charge experiments were performed over a voltage range of 1.0–3.0 V (vs. Li⁺/Li) at various rates using a LAND CT2001A battery tester. Electrochemical impedance spectroscopy (EIS) measurements were carried out on an Autolab PGSTAT302N electrochemical workstation by applying a sine wave with the amplitude of 10.0 mV over the frequency range from 100 kHz to 10 mHz. Cyclic voltammetry (CV) tests were performed using the same workstation as EIS measurements at a scanning rate of 0.1 mV s⁻¹.

3. Results and discussions

The XRD patterns of the H-TiO₂(B) and A-TiO₂(B) nanostructures are shown in Fig. 1, where it is compared with standard monoclinic
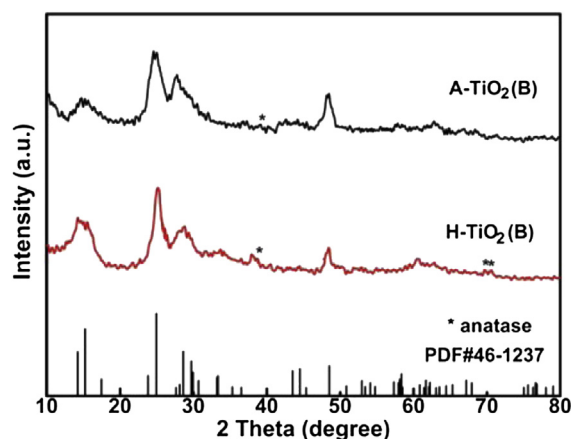
Fig. 1. XRD patterns of the H-TiO₂(B) and A-TiO₂(B) nanostructures. Bulk TiO₂(B) from the JCPDS database is shown for comparison.
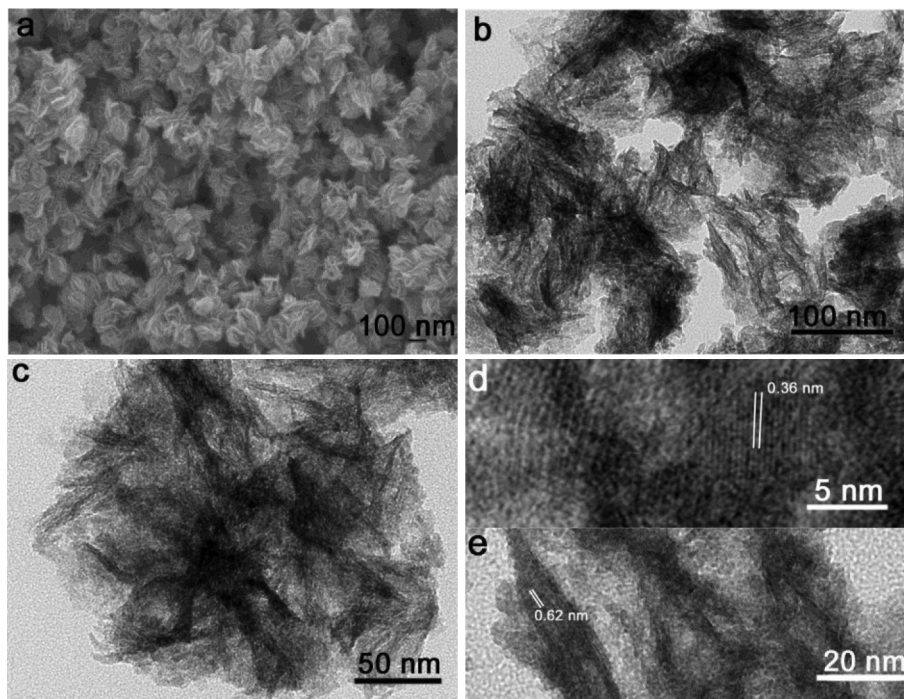
Fig. 2. SEM (a), TEM (b and c) and HRTEM (d) images of H-TiO$_2$(B) nanostructures.

TiO$_2$(B) (JCPDS card no. 46-1237). The diffraction peaks of the H-TiO$_2$(B) and A-TiO$_2$(B) nanostructures are broadened, indicating the small size of the flower-like TiO$_2$(B) nanostructures, but the powder diffraction patterns follow the same intensity distribution as that of the standard material. Some minor peaks can be identified as tetragonal anatase phase (JCPDS card no. 21-1272), which is obtained from the partial transformation of TiO$_2$(B) during heat treatment.

The sizes and morphologies of H-TiO$_2$(B) and A-TiO$_2$(B) nanostructures are characterized by the SEM, TEM, and HRTEM analysis. The as-synthesized H-TiO$_2$(B) nanostructures show a flower-like morphology, which are hierarchical and further composed of primary nanosheets with a thickness of several to ten nanometers (Fig. 2a). It is worth noting that the solvothermal precursors (Fig. S1a) and the A-TiO$_2$(B) nanostructures (Fig. S1b) show the similar morphology as that of H-TiO$_2$(B) nanostructures, indicating the flower-like morphology derived from the solvothermal products are stable and well maintained after hydrogenation treatment. TEM images in Figs. 2b and S1c further reveal the flower-like features of H-TiO$_2$(B) and A-TiO$_2$(B) nanostructures. A single flower-like H-TiO$_2$(B) nanostructure is shown in Fig. 2c, which is in a diameter of about 124 ± 5 nm and composed of several thin nanosheets with only 10 ± 1.2 nm in thickness. HRTEM images of H-TiO$_2$(B) nanostructure (Fig. 2d and e) and A-TiO$_2$(B) nanostructures (Fig. S1d) show that the single nanosheet is polycrystalline with clear mesopores, which are helpful for the diffusion of Li$^+$. The observed fringes correspond to the interplanar distances of 0.36 (Fig. 2d) and 0.62 nm (Fig. 2e), which are in good agreement with the lattice spacing of the (110) and (001) planes of monoclinic TiO$_2$(B), respectively.

XPS analysis was performed to examine the effect of hydrogenation on the chemical composition and oxidation state of TiO$_2$(B) nanostructures. Fig. 3 shows the XPS survey spectra of H-TiO$_2$(B) and A-TiO$_2$(B) nanostructures. It can be clearly seen that both show the similar sharp and peak intensity, indicating high purity of the as-synthesized materials (Fig. 3a). The upper panel of Fig. 3b shows the normalized Ti 2p core level XPS spectra of H-TiO$_2$(B) and A-

TiO$_2$(B) nanostructures. From the spectra of A-TiO$_2$(B) nanostructures, two broad peaks centered at 465.1 and 458.9 eV are observed, which correspond to the characteristic Ti 2p$_{1/2}$ and Ti 2p$_{3/2}$ peaks of Ti^{4+} species, respectively [29–32]. In comparison with A-TiO$_2$(B), the peaks of the H-TiO$_2$(B) sample show a negative shift in binding energy, indicating that it has different bonding environments. By subtracting the normalized Ti 2p spectra of H-TiO$_2$(B) with A-TiO$_2$(B) sample (lower panel of Fig. 3b), two extra peaks centered at ca. 463.4 and 457.8 eV are observed, which are consistent with the characteristic Ti 2p$_{1/2}$ and Ti 2p$_{3/2}$ peaks of Ti^{3+} species [33,34]. These results confirm the presence of Ti^{3+} species in the H-TiO$_2$(B) nanostructures and also suggest that oxygen vacancies (Ti^{3+} sites) are created in H-TiO$_2$(B) nanostructures during the hydrogen reduction process. The color change (Fig. S2) of the samples from white to dark yellow is in good agreement with these results. As shown in Fig. 3c and d, the O 1s spectra of both samples are asymmetric and exhibit a broad shoulder to the high binding energy side, indicating that several oxygen species are present in the near surface region. The O 1s spectra can be deconvoluted by four asymmetric Gaussian curves. The two main peaks at about 529.6–530.0 eV are attributed to oxygen in the anatase TiO$_2$ and TiO$_2$(B) crystal lattice (O$_{L1}$ and O$_{L2}$), respectively [19,35]. The other two broad oxygen peaks can be assigned to the Ti–O bonds of Ti$_2$O$_3$ (O$_{Ti3+}$, 531.0 eV) and the hydroxyl groups (O$_H$, 532.1 eV), respectively [35,36]. Table S1 summits the results of curve-fitting of the high resolution XPS spectra for the O1s region. For the H-TiO$_2$(B), the O$_{Ti3+}$ content and the O$_H$ content are, respectively, calculated to be 14.7 and 4.4%, while for the A-TiO$_2$(B), the contents of O$_{Ti3+}$ and O$_H$ are 0.54 and 2.8%, respectively. The higher O$_{Ti3+}$ content means a higher content of donor density of H-TiO$_2$(B) nanostructures, which dramatically increase the electronic conductivity of TiO$_2$(B) by several orders of magnitude, up to 2.79×10^{-3} S cm^{-1} compared to that of A-TiO$_2$(B) nanostructures (8.34×10^{-10} S cm^{-1}). In addition, a higher density of hydroxyl groups is beneficial for modifying the surface electrochemical activity and the pseudocapacitive performance of H-TiO$_2$(B).
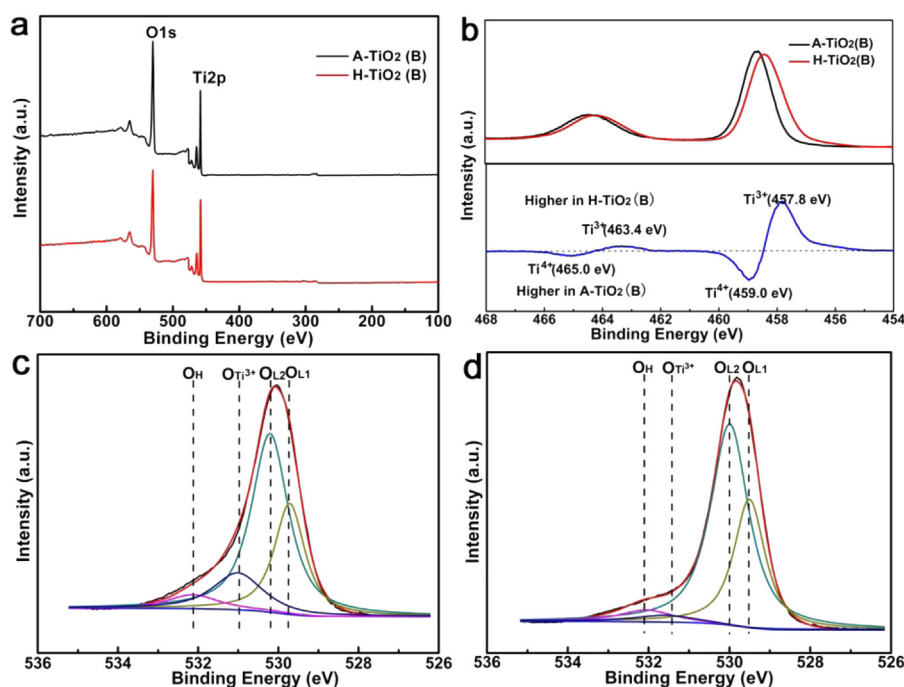
Fig. 3. XPS survey spectra of the H-TiO$_2$(B) and A-TiO$_2$(B) nanostructures (a) and normalized Ti 2p core level XPS spectra of H-TiO$_2$(B) and A-TiO$_2$(B) nanostructures together with their difference spectrum (b); O1s core level XPS spectra of H-TiO$_2$(B) nanostructures (c) and A-TiO$_2$(B) nanostructures (d).

To investigate the effect of hydrogenation on the electrochemical properties of TiO$_2$(B), the CV, galvanostatic discharge–charge, and EIS tests are performed and evaluated in lithium half-cells. CV measurements were employed to investigate the phase transformation and ionic diffusion process during the electrode reactions. Fig. 4a compares the CV curves of the H-TiO$_2$(B) and A-TiO$_2$(B) electrodes at a scanning rate of 0.1 mV s^{-1} in the potential window of 1.0–3.0 V (vs. Li$^+$/Li). There are three pairs of peaks in the CV curve of H-TiO$_2$(B) and A-TiO$_2$(B) electrodes. Two pairs of S-peaks at ca. 1.45 V/1.54 V and 1.55 V/1.68 V are assigned to the pseudocapacitive lithium storage behavior of TiO$_2$(B) while a pair of A-peaks at 1.7 V/2.0 V are assigned to the solid-state lithium diffusion of anatase TiO$_2$, which are consistent with TiO$_2$(B) species as reported previously [10,11,17–19]. By comparing the CV curve with that of the A-TiO$_2$(B) electrode, the peak shape of the H-TiO$_2$(B) electrode is sharper and intense, and the gap between the redox peaks is smaller, demonstrating that the latter exhibits better electrode kinetics and reversibility due to a lower degree of polarization of the electrodes during the electrochemical reaction. Fig. 4b shows the typical charge and discharge profiles of the H-TiO$_2$(B) electrode cycled at different current rates from 0.5C to 10C in the potential range of 1.0–3.0 V. It delivers a reversible discharge capacity of 292.3 mA h g^{-1} at the initial lower rate of 0.5C, which is close to its theoretical capacity of 335 mA h g^{-1}. Two distinct plateaus appear at 1.75 and 1.90 V in the low-rate (0.5C) charge–discharge curve, respectively, corresponding to the lithium insertion and de-insertion in the anatase TiO$_2$ phase. But the major capacities occur in the sloped regions of 1.75–1.0 V and 1.0–1.9 V. These results indicate the pseudocapacitance from TiO$_2$(B) is the predominate contribution of total capacity. With the increase of charge–discharge rates, the plateaus gradually diminish, which means H-TiO$_2$(B) nanostructures has the capability to maintain capacity by the fast pseudocapacitive process of lithium storage during the high-rate charge–discharge process. The discharge capacity of the H-TiO$_2$(B) electrode is slightly decreased as the charge–discharge rate increases from 1C to 10C, which delivers 256.1, 235.4, 208.2, and 179.6 mA h g^{-1} at a rate of 1, 2, 5, and 10C,

respectively. However, as shown in Fig. 4c, the A-TiO$_2$(B) electrode delivers discharge capacities of 271.6, 239.5, 207.1, 159.2, and 129.7 mA h g^{-1} at a rate of 0.5, 1, 2, 5, and 10C, respectively. The high rate capability of A-TiO$_2$(B) electrode is derived from the reduced size and porous structures, which can effectively shorten the transport paths of electrons and lithium ions, and simultaneously provide greater electrode/electrolyte contact area. Obviously, the H-TiO$_2$(B) electrode exhibits a much higher discharge capacity at various rates. Given that the morphologies of both TiO$_2$(B) nanostructures are similar, the improved rate capability in H-TiO$_2$(B) electrode should be due to the enhanced electronic conductivity of electrode. Fig. 4d compares the rate capability of the H-TiO$_2$(B) and A-TiO$_2$(B) electrodes. It is found that the storage capacities of both electrodes are stable at each current rate except 0.5C. When the current rate reverses back to 0.5C, their discharge capacities can recover to the original value immediately, indicating that the electrode materials possess high structure stability even after high rate cycling.

Fig. 5 gives the long-term cycling performance and the Coulombic efficiency of the H-TiO$_2$(B) and A-TiO$_2$(B) electrodes at a high current rate of 10C. In the case of the hydrogenated sample, the initial capacity is 179.9 mA h g^{-1}, which decreases to 177.1 mA h g^{-1} after 200 cycles, with a good capacity retention of 98.4%. However, for the pristine sample, the initial capacity is 130.1 mA h g^{-1}, which decreases to 121.4 mA h g^{-1} after 200 cycles, with an inferior capacity retention of 93.4%. It should be noted that the Coulombic efficiency of both H-TiO$_2$(B) and A-TiO$_2$(B) electrodes is maintained almost 100% apart from the first several cycles.

EIS spectra of H-TiO$_2$(B) and A-TiO$_2$(B) electrode has been fit and analyzed to interrogate the kinetic process of electrode reactions. Fig. 6a shows the EIS curves and the fitted line of both TiO$_2$(B) nanostructures after 70 cycles of rate capability test at discharge states. Each of the curves consists of two depressed semicircle (at high frequency) and a straight line (at low frequency). The inset in Fig. 6a shows the equivalent circuits of H-TiO$_2$(B) and A-TiO$_2$(B) electrodes. In both cases, R_0 represents the uncompensated bulk resistance of the electrolyte, separator, and electrode; the ($C_{dl}R_1$)

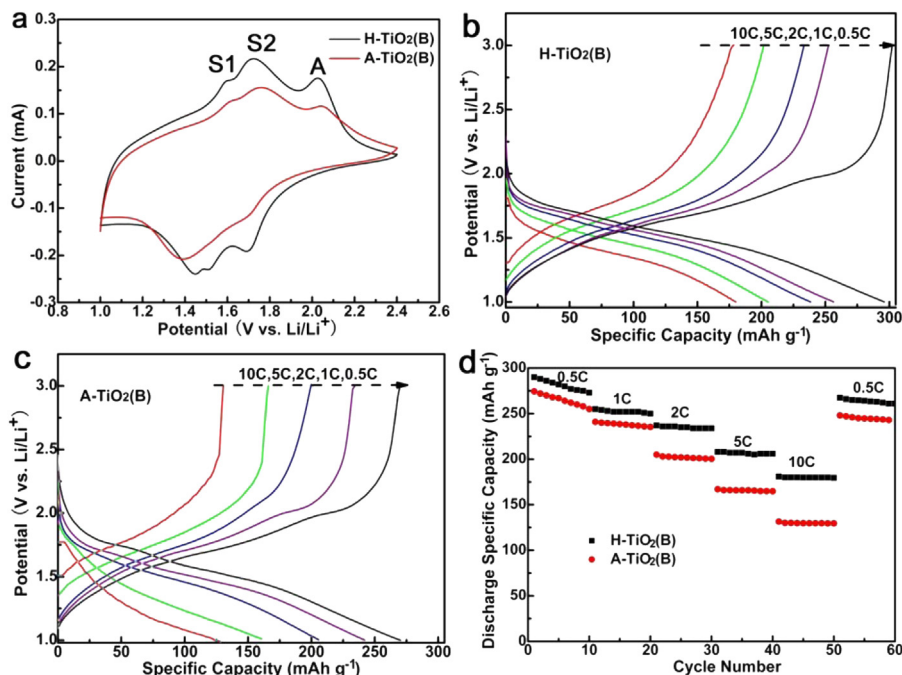**Fig. 4.** (a) CV curves of H-TiO$_2$(B) and A-TiO$_2$(B) electrodes at a scan rate of 0.1 mV s^{-1}. Galvanostatic discharge–charge profiles of H-TiO$_2$(B) electrode (b) and A-TiO$_2$(B) electrode (c) at various rates. (d) Comparison of the rate performance of H-TiO$_2$(B) electrode and A-TiO$_2$(B) electrode.
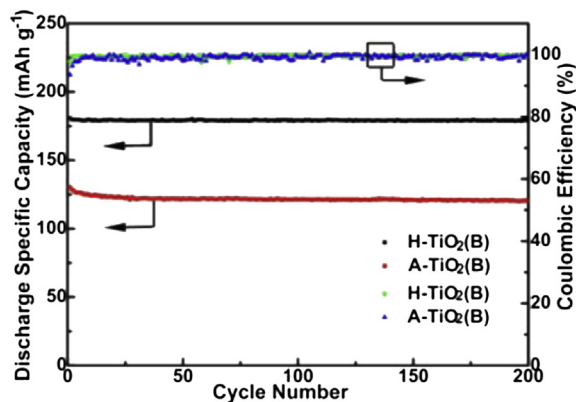

Fig. 5. The long-term cycling performances and the Coulombic efficiencies of H-TiO$_2$(B) and A-TiO$_2$(B) electrodes at 10C.

parallel element corresponds to the internal resistance of the TiO$_2$(B) materials and the double layer capacitance; and the (C_{ps}(R_{ct}W)) element is related to the charge transfer-limited process, pseudocapacitive effect from TiO$_2$(B) and the electronic and ionic diffusional-limited process. It should be stressed that both the impedance spectra hardly exhibits the Warburg impedance, which is associated with the semi-infinite diffusion of cations in the electrode. This is consistent with the previous researches which have proposed that the electrochemical lithium storage of TiO$_2$(B) materials is controlled by the mixed process of both the pseudocapacitive effect and diffusion-limited reaction [10,13]. It is obvious that the H-TiO$_2$(B) electrode exhibits a much lower R_{ct} value (35.8 Ω) than that of the A-TiO$_2$(B) electrode (61.2 Ω), mainly due to the enhanced electronic conductivity after the introduction of oxygen vacancies and/or Ti^{3+} species into the TiO$_2$(B) nanostructures. In addition to R_{ct}, the apparent lithium ion diffusion coefficient (D_{Li}) also has a noticeable synergistic effect. The values of D_{Li} are calculated from the inclined lines in the Warburg region in lower frequency ranges, based on the following equation: $D_{Li} = R^2T^2/$
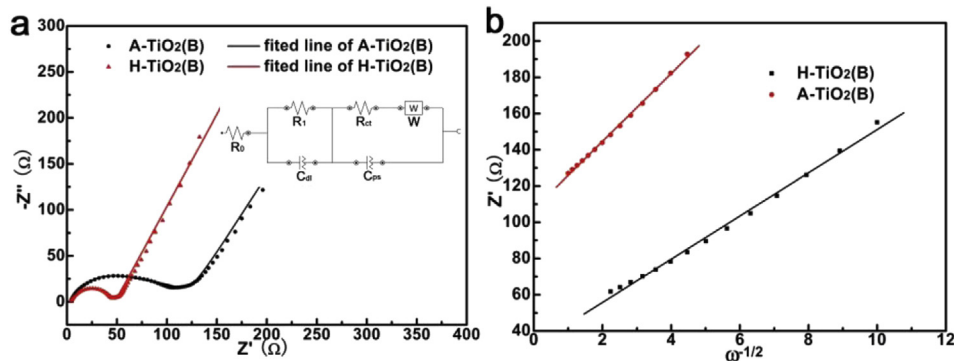

Fig. 6. EIS spectrum and their fitted lines (a) of H-TiO$_2$(B) electrode and A-TiO$_2$(B) electrode; inset: the equivalent circuits of both electrodes, where R_0 is the bulk resistance of the coin-cell, R_1 is the internal resistance of the TiO$_2$(B) electrode, R_{ct} is the charge transfer resistance, C_{dl} is the double layer capacitance, W is the Warburg diffusion resistance, C_{ps} is the pseudocapacitance from TiO$_2$(B). (b) The relation of Z′ (real) and $\omega^{-1/2}$ at low frequency.

$2A^2n^4F^4C^2\sigma^2$, or where R is the gas constant, T is the absolute temperature, A is the surface area of the anode electrode, n is the number of electrons per molecule during oxidization, F is the Faraday constant, C is the lithium concentration and σ is the Warburg factor. The Warburg factors s for both electrodes are determined by plotting in the complex plane $-Z'$ (real) $= \sigma \times \omega^{-1/2}$ against $\omega^{-1/2}$ where ω is the angular frequency, which are presented in Fig. 6b. The D_{Li} value of the H-TiO$_2$(B) electrode is calculated to be 6.81×10^{-13} cm^2 s^{-1}, which is about two times higher than that of A-TiO$_2$(B) electrode (3.50×10^{-13} cm^2 s^{-1}). The excellent rate capability of H-TiO$_2$(B) electrode is attributed to the enhanced electronic conductivity and the modified surface electrochemical activity after introducing oxygen vacancies (Ti^{3+} species) and hydroxyl groups into the TiO$_2$(B) nanostructures.

4. Conclusions

In conclusion, we have employed a combined solvothermal and hydrogenation treatment process to successfully synthesize flower-like hydrogenated TiO$_2$(B) nanostructures. The thin primary TiO$_2$(B) nanosheets are in a thickness of 10 ± 1.2 nm, which is helpful for the facilitation of Li$^+$. The introduction of Ti^{3+} species and/or oxygen vacancies greatly improves the electronic conductivity (up to 2.79×10^{-3} S cm^{-1}). As expected, the H-TiO$_2$(B) nanostructures exhibit improved lithium ion storage performance including higher specific capacity, superior rate performance and better cycling stability in comparison with the pristine A-TiO$_2$(B) nanostructures. The facile hydrogenation method can be expected to open up opportunities in designing high-performance electrode materials with semiconductor features for lithium ion batteries.

Acknowledgment

Appendix A. Supplementary data

Supplementary data related to this article can be found at http://dx.doi.org/10.1016/j.jpowsour.2014.05.121.

References

[1] J.M. Tarascon, M. Armand, Nature 414 (2001) 359–367.
[2] V. Etacheri, U. Geiger, Y. Gofer, G.A. Roberts, I.C. Stefan, R. Fasching, D. Aurbach, Langmuir 28 (2012) 6175–6184.
[3] M. Armand, J.M. Tarascon, Nature 451 (2008) 652–657.
[4] P.G. Bruce, B. Scrosati, J.M. Tarascon, Angew. Chem. Int. Ed. 47 (2008) 2930–2946.
[5] A.G. Dylla, J.A. Lee, K.J. Stevenson, Langmuir 28 (2012) 2897–2903.
[6] K. Saravanan, K. Ananthanarayanan, P. Balaya, Energy Environ. Sci. 3 (2010) 939–948.
[7] M. Wagemaker, W.J.H. Borghols, F.M. Mulder, J. Am. Chem. Soc. 129 (2007) 4323–4327.
[8] J. Wang, Y. Bai, M. Wu, J. Yin, W.F. Zhang, J. Power Sources 191 (2009) 614–618.
[9] Z. Hong, M. Wei, T. Lan, G. Cao, Nano Energy 1 (2012) 466–471.
[10] H. Liu, Z. Bi, X. Sun, R.R. Unocic, M.P. Paranthaman, S. Dai, G.M. Brown, Adv. Mater. 23 (2011) 3450–3454.
[11] S. Liu, Z. Wang, C. Yu, H. Bin Wu, G. Wang, Q. Dong, J. Qiu, A. Eychmüller, X.W. Lou, Adv. Mater. 25 (2013) 3462–3467.
[12] Z. Zhang, G. Li, H. Peng, K. Chen, J. Mater. Chem. A 1 (2013) 15429–15434.
[13] G. Zhu, Y. Wang, Y. Xia, Energy Environ. Sci. 5 (2012) 6652–6667.
[14] M. Zukalová, M. Kalbáč, L. Kavan, I. Exnar, M. Graetzel, Chem. Mater. 17 (2005) 1248–1255.
[15] A.R. Armstrong, G. Armstrong, J. Canales, R. García, P.G. Bruce, Adv. Mater. 17 (2005) 862–865.
[16] A.G. Dylla, G. Henkelman, K.J. Stevenson, Acc. Chem. Res. 46 (2013) 1104–1112.
[17] Y. Ren, Z. Liu, F. Pourpoint, A.R. Armstrong, C.P. Grey, P.G. Bruce, Angew. Chem. Int. Ed. 51 (2012) 2164–2167.
[18] S. Liu, H. Jia, L. Han, J. Wang, P. Gao, D. Xu, J. Yang, S. Che, Adv. Mater. 24 (2012) 3201–3204.
[19] S. Brutti, V. Gentili, H. Menard, B. Scrosati, P.G. Bruce, Adv. Energy Mater. 2 (2012) 322–327.
[20] J. Li, W. Wan, H. Zhou, J. Li, D. Xu, Chem. Commun. 47 (2011) 3439–3441.
[21] J. Liu, X.W. Liu, Adv. Mater. 24 (2012) 4097–4111.
[22] Y.F. Tang, L. Yang, Z. Qiu, J.S. Huang, Electrochem. Commun. 10 (2008) 1513–1516.
[23] T. Yang, Y. Chen, B. Qu, L. Mei, D. Lei, H. Zhang, Q. Li, T. Wang, Electrochim. Acta 115 (2014) 165–169.
[24] W.J. Zhou, H. Liu, R.I. Boughton, G.J. Du, J.J. Lin, J.Y. Wang, D. Liu, J. Mater. Chem. 20 (2010) 5993–6008.
[25] J. Shin, J.H. Joo, D. Samuelis, J. Maier, Chem. Mater. 24 (2012) 543–551.
[26] Z. Zheng, B. Huang, X. Meng, J. Wang, S. Wang, Z. Lou, Z. Wang, X. Qin, X. Zhang, Y. Dai, Chem. Commun. 49 (2013) 868–870.
[27] Y. Yan, B. Hao, D. Wang, G. Chen, E. Markweg, A. Albrecht, P. Schaaf, J. Mater. Chem. A 1 (2013) 14507–14513.
[28] G. Li, Z. Zhang, H. Peng, K. Chen, RSC Adv. 3 (2013) 11507–11510.
[29] S.T. Myung, M. Kikuchi, C.S. Yoon, H. Yashiro, S.J. Kim, Y.K. Sun, B. Scrosati, Energy Environ. Sci. 6 (2013) 2609–2614.
[30] X. Jiang, Y. Zhang, J. Jiang, Y. Rong, Y. Wang, Y. Wu, C. Pan, J. Phys. Chem. C 116 (2012) 22619–22624.
[31] A. Naldoni, M. Allieta, S. Santangelo, M. Marelli, F. Fabbri, S. Cappelli, C.L. Bianchi, R. Psaro, V.D. Santo, J. Am. Chem. Soc. 134 (2012) 7600–7603.
[32] M.S. Lazarus, T.K. Sham, Chem. Phys. Lett. 92 (1982) 670–674.
[33] F. Werfel, O. Brummer, Phys. Scr. 28 (1983) 92–96.
[34] E. McCafferty, J.P. Wightman, Surf. Interface Anal. 26 (1998) 549–564.
[35] J. Zhuang, S. Weng, W. Dai, P. Liu, Q. Liu, J. Phys. Chem. C 116 (2012) 25354–25361.
[36] J.C. Yu, J. Yu, H.Y. Tang, L. Zhang, J. Mater. Chem. 12 (2002) 81–85.